Radio Science, Volume 33, Number 3, Pages 753–766, May–June 1998

A global high-resolution microwave emission model for the Earth

G. Schiavon, P. Ferrazzoli, and D. Solimini

Dipartimento di Informatica, Sistemi e Produzione, Università Tor Vergata, Rome, Italy

P. de Maagt and J.P.V. Poiares Baptista

European Space Agency, European Space Research and Technology Centre, Noordwijk, Netherlands

Abstract. This paper reports on a numerical model developed to simulate vertically and horizontally polarized microwave emission from the Earth in the frequency range between 5 and 50 GHz and at various angles of observation, with a 1° × 1° (latitude by longitude) spatial resolution, taking into account seasonal variations. The principal motivation of the model is the evaluation of the noise antenna temperature of telecommunications satellites, which is required to calculate the uplink G/T for satellite-borne receivers. The results of the study, however, prove useful in a number of remote sensing applications. To implement the model, significant types of surface, such as bare soil, nonarboreous vegetation, forests, snow, glacier and sea ice, and ocean, have been identified, and their emissivity properties have been determined by the available theoretical and/or empirical models. The millimeter-wave propagation model of *Liebe* [1993] has been used to compute the atmospheric contribution. Profiles from actual radio soundings collected during a 10-year period over the globe have been used to take into account major climatic variations. The various contributions from the surface and the atmosphere have been finally combined to obtain the theoretical global brightness temperature of each 1° × 1° pixel. The numerical model has been validated by comparing on a pixel-by-pixel basis the theoretical brightness temperature with those measured by the special sensor microwave imager (SSM/I) radiometer in the year 1992 at 19.35, 22.235, and 37.0 GHz at the available polarizations. The discrepancies between model and experimental brightness temperatures have been noted, and actions have been taken to reduce the differences. In its present configuration, the global emission model yields brightness temperature estimates which differ all over the Earth by less than 12 K rms from those measured by the SSM/I.

1. Introduction

Experience from existing telecommunications satellites shows that large (exceeding 2 dB) discrepancies often exist between the predicted and the in-orbit measured satellite uplink gain-to-noise ratio G/T. The basic reason for these discrepancies is believed to lie in the estimate of the system noise temperature T, which is usually performed assuming a fixed satellite antenna temperature $T_A = 290$ K. When the repeater noise is high, its contribution to the system temperature is predominant, and the above assumption has little bearing on the accuracy of the estimate. However, since with improved technology the noise of repeaters has decreased, T_A tends to become a crucial parameter, and the correctness of its estimate can substantially affect the accuracy of the predicted G/T.

The temperature of a satellite antenna aimed at Earth can be predicted by

$$T_A = \frac{1}{4\pi} \int_{4\pi} \left[T_B^{\mathrm{NS}}(a, b, \theta)\, D^{\mathrm{NS}}(\psi, \phi) + T_B^{\mathrm{EW}}(a, b, \theta)\, D^{\mathrm{EW}}(\psi, \phi) \right] d\Omega \qquad (1)$$

where angles ψ and ϕ denote the direction from which the emitted power comes; $a(\psi, \phi)$ and $b(\psi, \phi)$ are the corresponding latitude and longitude of the Earth's surface parcel where emission originates; $\theta(\psi, \phi)$ is the angle with respect to the local zenith; $D^{\mathrm{NS}}(\psi, \phi)$ and $D^{\mathrm{EW}}(\psi, \phi)$ are the antenna directivity functions for the two N–S and E–W orthogonal polarizations; and $T_B^{\mathrm{NS}}(a, b, \theta)$ and $T_B^{\mathrm{EW}}(a, b, \theta)$ are the corresponding brightness temperatures of the Earth.

Paper number 97RS02304.
0048-6604/98/97RS-02304$11.00

Equation (1) indicates that the accuracy of the estimate depends on the faithfulness of the available model in reproducing the actual features of the apparent Earth's brightness temperature $T_B^i(a, b, \theta)$. A simple first model, usable for wide-beam antennas, was developed by the European Space Agency (ESA) [*de Maagt et al.*, 1994; *Fenech et al.*, 1995]. Use of this model allowed the reduction of the discrepancy between G/T prediction and in-orbit measurements of EUTELSAT II F4 to slightly more than 1 dB. However, even for the relatively wide beam of this satellite, appreciable differences between the receive coverage computed from the predicted antenna temperature and the measured one still appeared. Moreover, the ESA/EUTELSAT model neglected several features of the apparent temperature (e.g., the dependence on θ), assumed simple spatial distributions (i.e., continents were assumed to be of uniform T_B), and was developed for a single frequency. Consequently, a more refined and comprehensive model of $T_B^i(a, b, \theta)$ was desirable to enhance the prediction accuracy for satellite systems operating in a wide frequency range, at any orbital location (including nongeostationary ones) and using narrow-beam antennas, too.

The following reports a more realistic model of emission of the Earth that has been developed to simulate the spatial distribution of the microwave brightness temperature observed by a satellite antenna. The model is based on a physical approach and strives to include all factors of the terrestrial environment that are relevant to an accurate estimate of microwave emission. For this reason, we follow a comprehensive approach, avoiding unnecessary simplifications which would unavoidably decrease the accuracy of estimates.

The brightness temperature observed by a satellite-borne antenna observing the surface at an off-zenith angle θ, at frequency f, and in q polarization (in the following, $p = 1$ (horizontal), 2 (vertical) and $q = 1, 2$ indicate polarization state) is given by

$$T_B^q(f,\theta) = T_{UP}(f,\theta) + \frac{1}{L_a(f,\theta;0,\infty)}[T_{Bs}^q(f,\theta) + T_{SC}^q(f,\theta)] \quad (2)$$

where

$$T_{Bs}^q(f,\theta) = T_S e_q(f,\theta) \quad (3)$$

is the brightness temperature of the surface and $e_q(f,\theta)$ and T_S are its emissivity and thermodynamic temperature, respectively;

$$T_{UP}(f,\theta) = \sec\theta \int_0^\infty T(z)\alpha(f,z)e^{-\sec\theta \int_{z'}^\infty \alpha(f,z')dz'} dz \quad (4)$$

is the upward brightness temperature of the atmosphere, with $T(z)$ and $\alpha(f,z)$ denoting its thermodynamic temperature and absorption coefficient, respectively, at height z;

$$T_{SC}^q(f,\theta) = \frac{1}{4\pi\cos\theta}\int_0^{\pi/2} T_{DN}(f,\theta_s)\times \left[\int_0^{2\pi}\sum_{p=1}^{2}\sigma_{qp}^0(f,\theta,\theta_s,\phi_s)d\phi_s\right]\sin\theta_s d\theta_s \quad (5)$$

is the surface-scattered contribution, representing the portion of the atmospheric downward emitted radiation $T_{DN}(f,\theta)$ that is scattered toward the satellite antenna by the surface, where $\sigma_{qp}^0(f,\theta,\theta_s,\phi_s)$ is its bistatic scattering coefficient;

$$T_{DN}(f,\theta_s) = \sec\theta\int_0^\infty T(z)\alpha(f,z)e^{-\sec\theta\int_0^{z'}\alpha(f,z')dz'}dz + T_{\cos}e^{-\sec\theta\int_0^\infty\alpha(f,z)dz} \quad (6)$$

with $T_{\cos}$ denoting the cosmic background;
and

$$L_a(f,\theta;0,\infty) = e^{\sec\theta\int_0^\infty\alpha(f,z)dz} \quad (7)$$

is the attenuation introduced by the atmospheric path.

A useful approximation, which substantially reduces the computation time and will be used in the following, calculates the contribution of the scattered downwelling power through an effective specular reflection [*Ulaby et al.*, 1986]. In this case

$$T_{SC}^q(f,\theta) \simeq [1 - e_q(f,\theta)]\,T_{DN}(f,\theta) \quad (8)$$

The above equations point out that the brightness temperature observed by the antenna results from contributions by the surface and the atmosphere, including interactions. These contributions depend on type and state of both surface and atmosphere and vary with geographical location and season. Hence reliable emission modeling has to be based on the physical characteristics of the surface and atmosphere.

The global emission model that has been developed is based on a detailed ($1° \times 1°$ latitude by longitude) description of the local surface and on its characterization from the emissivity point of view. The local emitting and attenuating properties of the overlying atmosphere and the surface-atmosphere interaction are also incorporated to determine the overall emission. The relevant information on the local surface has been derived from

the NASA Global Data Sets [*Meeson et al.*, 1995; *Sellers et al.*, 1995] and the Distributed Active Archive Centre (DAAC) Interdisciplinary Data Collection (NASA), while for the atmosphere, the Fondazione Ugo Bordoni (FUB) and ESA Radiosonde and Surface (FERAS) data base was used [*Barbaliscia et al.*, 1995]. (The NASA Interdisciplinary Data Collection is available via anonymous ftp at daac.gsfc.nasa.gov.)

The frequency limits (5–50 GHz) considered by the model include the main telecommunications frequency bands (C, K_u, and K_a); the range of observation angles (i.e., the angle from the local zenith) up to 87.5° is able to cover any orbital location; and the $1° \times 1°$ spatial resolution allows regional beam evaluations, too.

It should be pointed out that this model may also prove useful in a number of remote sensing applications, mainly involving large-scale effects. Among others, we can cite the understanding of low-resolution satellite data characteristics, the screening of satellite radiometric data for precipitation identification [*Wilheit et al.*, 1994], and the prediction of the performance of next-generation satellite radiometric systems.

2. Emission from the Earth Surface

To model the power density emitted at microwave frequencies from the Earth's surface in the various seasons, the significant surface categories present on the planet have to be identified and their emissivity estimated. For each category, emission depends both on the receiving system parameters (frequency, angle, and polarization) and on the surface time-dependent physical properties. These affect the permittivity and the geometric structure in a way which is different among the various cases; hence the contribution to the antenna noise power is peculiar of both the particular surface type and its state.

2.1. Identification of Surface Types

The whole surface of the Earth has been subdivided into $1° \times 1°$ (latitude by longitude) parcels, and the nature of the surface within each pixel has been identified. Seasonal variations have been taken into account by considering four different data sets, each referring to a period of 3 months, i.e., boreal spring (March–May), boreal summer (June–August), boreal autumn (September–November), and boreal winter (December–February).

First, land pixels have been separated from sea pixels by using the land/sea mask provided by *Meeson et al.* [1995]. In turn, the sea parcels have been subdivided into water, first-year, and multiyear ice, according to the 2-year data set provided by A. Nomura and R. Grumbine (personal communication, 1995). We have averaged the data over the four "seasons," thus obtaining an estimate of the seasonal sea ice concentration: The pixels having 100% of area permanently covered by ice irrespective of season have been considered multiyear ice, while the others have been assumed to be a mixed surface of first-year ice and sea water.

The characterization of the land parcels has been carried out based on the NASA global land cover classification data set [*DeFries and Townshend*, 1994]. This set allows desert, bare ground, water bodies, and continental ice to be separated from vegetation covers. Moreover, it provides 12 classes of vegetation covers; some of them are of permanent type, such as evergreen broadleaf and coniferous forests, while others exhibit seasonal cycles, like agricultural vegetation. Therefore an additional database, containing the monthly means of the leaf area index (LAI) [*Sellers et al.*, 1994, 1996], has been used to draw the vegetation information relevant to this work. Arboreous vegetation has been subdivided into two classes, i.e., dense and sparse, which, following a synthetic aperture radar (SAR) sensitivity analysis [*Imhoff*, 1995], may be chosen as reference forests for emissivity computation. In turn, the 2-year values of LAI averaged over the 3-month "seasons" give an indication of the density of nonarboreous vegetation (dense or sparse) to use in the seasonal computations of emissivity. The effects of soil roughness and moisture content have also been taken into account by introducing additional classes of "sparse" vegetation over dry and wet soils. Finally, the global snow depth database [*Foster and Davy*, 1988], which reports the midmonthly mean snow depth, has been used on the usual seasonal basis to introduce the eventual snow cover into the emissivity computations. Over the high-latitude regions in North America, Europe, and Asia, dry snow has been generally assumed in winter and wet snow has been assumed in spring. Mixed-type pixels have also been occasionally introduced, when needed to reduce the noted discrepancies between theoretical and experimental values.

2.2. Emissivity Models

To model emissivity, results obtained by the remote sensing community in the last decades are fundamental. Experimental data collected by ground-based, airborne, and spaceborne radiometers, as well as theoretical models and empirical models, are available. However, a systematic and extensive emissivity estimate cannot be achieved using only experimental data, nor using only theoretical models. Experimental data, in spite of several efforts,

have been obtained only in limited ranges of sensor parameters and do not cover uniformly the various Earth regions. On the other hand, models can, in principle, give emissivity estimates at all frequencies and angles; however, they are always based on simplified schemes of the real physical surface, so that to produce reliable quantitative estimates of emissivity, some parameters must be tuned against experimental data. In the present work, we have used both experimental data and models available in literature, generally adopting a mixed approach. For some surface types, like snow, for which extensive measurements were available, we have generated simple emission numerical algorithms based on interpolation and extrapolation of experimental data. In other cases we have used electromagnetic models, after validation over the available, generally limited, experimental data sets.

It must be stressed that experimental and theoretical efforts carried out by the remote sensing community concentrated on limited ranges of frequencies and angles, which appeared to be optimal for retrieving the biophysical and geophysical variables of interest, whereas, for the purpose of this work, wide ranges of these parameters are required. Therefore, since the results had to be extrapolated to cover the desired ranges of frequencies and angles, the reliability of our model becomes lower where results are scarce, like for $f > 37$ GHz and, particularly at angles higher than around 70°, where no experimental data are available and model uncertainties become important.

In the following, the emission properties of the various surface categories will be considered. For each category, the experimental and theoretical results which appear helpful to our purposes will be indicated and the approach selected to estimate the emissivity will be summarized. We consider numerous types of surface, and hence it would have been difficult to report the analytical details of the corresponding models, often composite and complicated, in this paper. Rather, the interested reader is referred to the cited literature.

2.2.1. Bare soil. From an electromagnetic point of view, bare soil may be considered as a lossy dielectric half-space with rough interfaces. Its emissivity depends on the surface roughness and the permittivity, which depends on soil moisture.

Emissivity measurements at 5 and 10 GHz were carried out by *Wang et al.* [1983] over a smooth and a rough soil, and results are also given by *Ulaby et al.* [1986]. *Paloscia et al.* [1993] reported results of measurements carried out at 10 and 36 GHz over two dry, rough soils and over a soil moistened and smoothed by artificial rain.

Among the theoretical models for emissivity, we have adopted the geometric optics (GO) model, which, according to the limits of validity given by *Ulaby et al.* [1982], is the most suitable when $f > 5$ GHz. Although some surface parameters, such as the top-layer moisture content and the roughness correlation length, are difficult to evaluate [*Borgeaud et al.*, 1995], the agreement between the adopted model and the experimental data published by *Wang et al.* [1983], *Paloscia et al.* [1993] and *Mätzler* [1994a] is reasonable.

2.2.2. Nonarboreous vegetation. The most frequently encountered kinds of nonarboreous vegetation are spontaneous vegetation in the form of grass, and agricultural crops. Microwave emission from this kind of vegetation may be viewed as that of a homogeneous half-space (soil) overlain by vegetation elements like stems, leaves, and ears. The emissivity depends on the stage of growth of the crops, the geometry of the vegetation elements, the roughness of the underlying soil, and the moisture content of soil and plants. At frequencies higher than 5 GHz and for developed crops, experimental and theoretical investigations demonstrate that the soil contribution to the overall emission is relatively low, so that the emissivity mainly depends on shape, orientation, dimensions, and permittivity of the vegetation elements [*Ferrazzoli and Guerriero*, 1995].

Similar to the case of soil, experimental data about vegetation emission at $f > 5$ GHz are relatively few, since the investigation efforts of the remote sensing community mainly concentrated on soil moisture retrieval. However, experiments carried out in Switzerland [*Wegmüller*, 1990] and Italy [*Pampaloni and Paloscia*, 1986; *Ferrazzoli et al.*, 1995] have produced an interesting and significant vegetation emission data set, particularly at X (10 GHz) and K_a (36 GHz) band. The results agree in indicating that developed wheat and barley crops, at high frequencies, behave similarly to black bodies, while sunflower and sugarbeet show the lowest emissivity. We have considered these two extreme cases and simulated the emission from wheat/barley and sunflower/sugarbeet crops using the vegetation model developed at Tor Vergata University [*Ferrazzoli et al.*, 1991a, b; *Ferrazzoli and Guerriero*, 1995].

As an example of the performance of the vegetation model, the theoretically predicted trends of emissivity with frequency at an angle of 50° are reported in Figure 1 for cereals (wheat/barley) and wide-leaf (sunflower/sugarbeet) vegetation types. The emissivity experimental data reported by *Mätzler* [1994a] for grass, shown for comparison, fall almost in the middle between

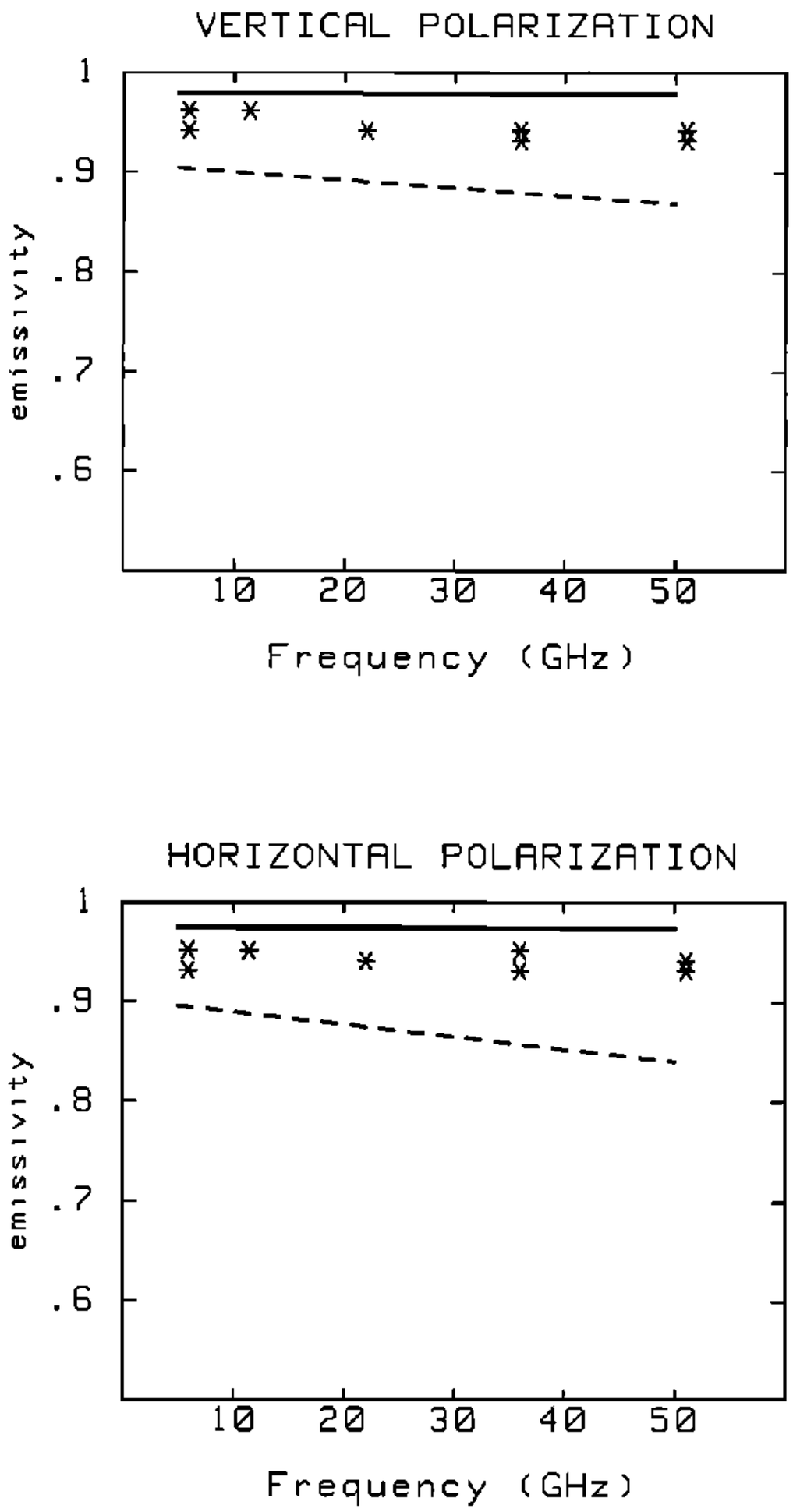

Figure 1. Predicted trends of emissivity versus frequency at 50° observation angle for wheat/barley (continuous lines) and sunflower/sugarbeet (dashed lines). Asterisks denote experimental data reported by *Mätzler* [1994a] for grass.

the two types, at both polarizations and the considered frequency range.

2.2.3. Arboreous vegetation. The remote sensing community considers monitoring forest parameters an objective of paramount importance. However, most of the work has been carried out by active systems (radars), so that experimental data regarding forest emission are very few. The emissivity of a pine forest was measured by a nadir-viewing multifrequency airborne radiometer in the former USSR [*Shutko and Chukhlantsev*, 1982]. Extensive multifrequency measurements of brightness temperature were carried out in Switzerland for coniferous and deciduous forests [*Sume et al.*, 1988]; in this case, the radiometers were ground-based and zenith-looking, so that the results may not be directly used to estimate the brightness temperature observed by a satellite.

To simulate emission from coniferous and deciduous forests, the model developed at Tor Vergata, whose results were successfully compared by *Ferrazzoli and Guerriero* [1996] and *Guerriero and Mätzler* [1995] with experimental data of *Shutko and Chukhlantsev* [1982] and *Sume et al.* [1988], has been used. The model describes forests as homogeneous half-spaces (soils) overlain by large vertical cylinders (trunks) and inclined cylinders (branches). Moreover, thin cylinders are introduced to simulate coniferous needles, while discs simulate deciduous leaves. According to model simulations, the emissivity in the range 10–50 GHz is practically constant and is higher for coniferous forests, where needle contribution dominates, than for deciduous forests, where leaf contribution dominates in summertime and twig contribution prevails when leaves have fallen down. At $f < 10$ GHz the branches become the main emission source, and the overall emissivity is reduced for both coniferous and deciduous forests.

2.2.4. Snow. A snow-covered surface may be regarded as a half-space (soil) overlain by a mixture of ice particles and air, or ice particles, liquid water, and air. The emission behavior depends primarily on the thickness of the snow layer but is also heavily affected by the physical structure of snow, which depends on the environmental and seasonal conditions of the surface. Various snow categories, like dry snow, wet snow, powder, and crust, characterized by appreciable differences in the emission behavior, have been identified [*Mätzler*, 1994a; *Noll et al.*, 1995]. We limit our analysis to the more common cases of dry and wet snow. Dry snow is a layer of ice particles whose dimensions are in the range 0.5–5 mm, while the characteristic dimension of water particles in wet snow is ~0.5 mm. As a consequence, particularly at high observation angles and horizontal polarization, the trends of emissivity with frequency of the two snow types are opposite to each other: Emissivity of wet snow increases with f, whereas that of dry snow decreases.

Physical models based on the radiative transfer theory have been proposed to simulate snow emission. These models, reviewed by *Fung* [1994], need input parameters generally difficult to measure. On the other hand, the experimental data set obtained in Switzerland [*Mätzler*, 1994a, b] is extensive, covering various snow conditions, various angles up to 75°, and a wide (4.9–94 GHz)

frequency range. Therefore we used the wet and dry snow results published by *Mätzler* [1994b] as a basis for our empirical estimation algorithm, interpolating in frequency and extrapolating at angles higher than 75° by a polynomial fitting.

2.2.5. Glacier and sea ice. Several experiments [*Ulaby et al.*, 1986] indicate that sea ice emission at the various frequencies is heavily dependent on ice age. The emissivity of first-year ice is relatively high at all frequencies, since the mixture of air, pure ice, and brine is characterized by a relatively low permittivity, while the snow layer which is generally present over it produces further absorption/emission. In the case of multiyear ice, emissivity is high at low frequencies but strongly decreases when the wavelength becomes comparable to the air bubble dimensions, due to increasing volume scattering.

To estimate the dependence on frequency of the emissivity of first-year ice, we have used the simple model of *Ulaby et al.* [1986], which assumes a homogeneous halfspace with a flat interface, composed by air, ice, and brine overlain by a snow layer. Modeling emission from multiyear ice is a complex task, since surface scattering originates from the air-snow and snow-ice interfaces, while air bubbles contribute toward volume scattering. In this case we have interpolated and extrapolated simulation results published by *Ulaby et al.* [1986], which appear to be in agreement with experimental data published by *Wilheit et al.* [1972] and *Troy et al.* [1981]. To simulate the emission of ice over land, which is generally lower than that of sea ice and has a different frequency dependence, observations by *Rott* [1989] have been used as the basis to implement an empirical model.

2.2.6. Ocean. Wind induces roughening of the water surface and the formation of foam. In principle, the effects of roughness on emissivity may be determined by surface scattering models similar to those used for bare soil, after establishing the relationship between roughness and wind speed. Foam may be regarded as an absorbing layer which reduces water reflectivity, producing an increase of emissivity. Extension and thickness of foam are functions of wind speed, while their effects are heavily dependent on frequency.

Several studies of ocean emission have been carried out, mostly using spaceborne scanning multichannel microwave radiometer (SMMR) data [*Hollinger*, 1971]. These studies have led to empirical and semiempirical models which reproduce the ocean emission as a function of frequency and wind speed [*Wilheit*, 1979; *Pandey and Kakar*, 1982].

Recently, a polarimetric emission model has been developed, based on a two-scale description of the sea surface height spectrum [*Coppo et al.*, 1996]. In this approach, emission originates from patches, affected by the small-scale roughness directly produced by the wind, which are tilted by the large-scale gravity waves. Emission from the tilted rough patches is computed by the small perturbation theory and modified to take the effect of foam into consideration through the empirical model of *Pandey and Kakar* [1982]. The results of the model have been validated against experimental data [*Dzura et al.*, 1994; *Yueh et al.*, 1995; *Trokhimovski et al.*, 1995] in the frequency range 3.7–36 GHz for various wind speeds.

The model, which incorporates a recent new model of sea water permittivity [*Ellison et al.*, 1996], allows computation of emission (as an average over azimuth) from the sea pixels, taking into account the seasonally averaged sea surface temperature [*Reynolds and Smith*, 1994] and wind speed [*Schubert et al.*, 1993].

As an example of model output as a function of surface parameters, Figure 2 shows the predicted brightness temperature of the ocean as a function of the 10-m-height wind speed for different frequencies. A decreasing trend of T_B with increasing speed is observed at frequencies $f \geq 40$ GHz. At these frequencies, no experimental data were available to ascertain whether such an effect is real or an artifact of the model.

3. Atmospheric Effects

In most of the considered frequency range, emission from each pixel of the Earth depends not only on the type of surface but also on the structure of the overlying atmosphere. Hence the model requires the identification of the moisture and thermal characteristics of the atmosphere over each 1° × 1° pixel.

Radiosonde data, kindly provided by F. Barbaliscia's group at Fondazione Ugo Bordoni, Rome, Italy [*Barbaliscia et al.*, 1995], have been used to model the atmospheric characteristics over the different locations. A total of 169 meteorological stations have been selected out of the FUB/ESA FERAS database, in order to generate a grid that at least over land, is dense enough to take possible significant climatic variations into account. Contours have been generated, surrounding each radiosonde launch site and shaped according to the homogeneity of the surface characteristics, and the corresponding 10-year (1980–1989) radiosonde profile data, averaged over the four 3-month periods, have been used to seasonally characterize the atmosphere over all parcels included within each contour. A major source of uncertainty stems from

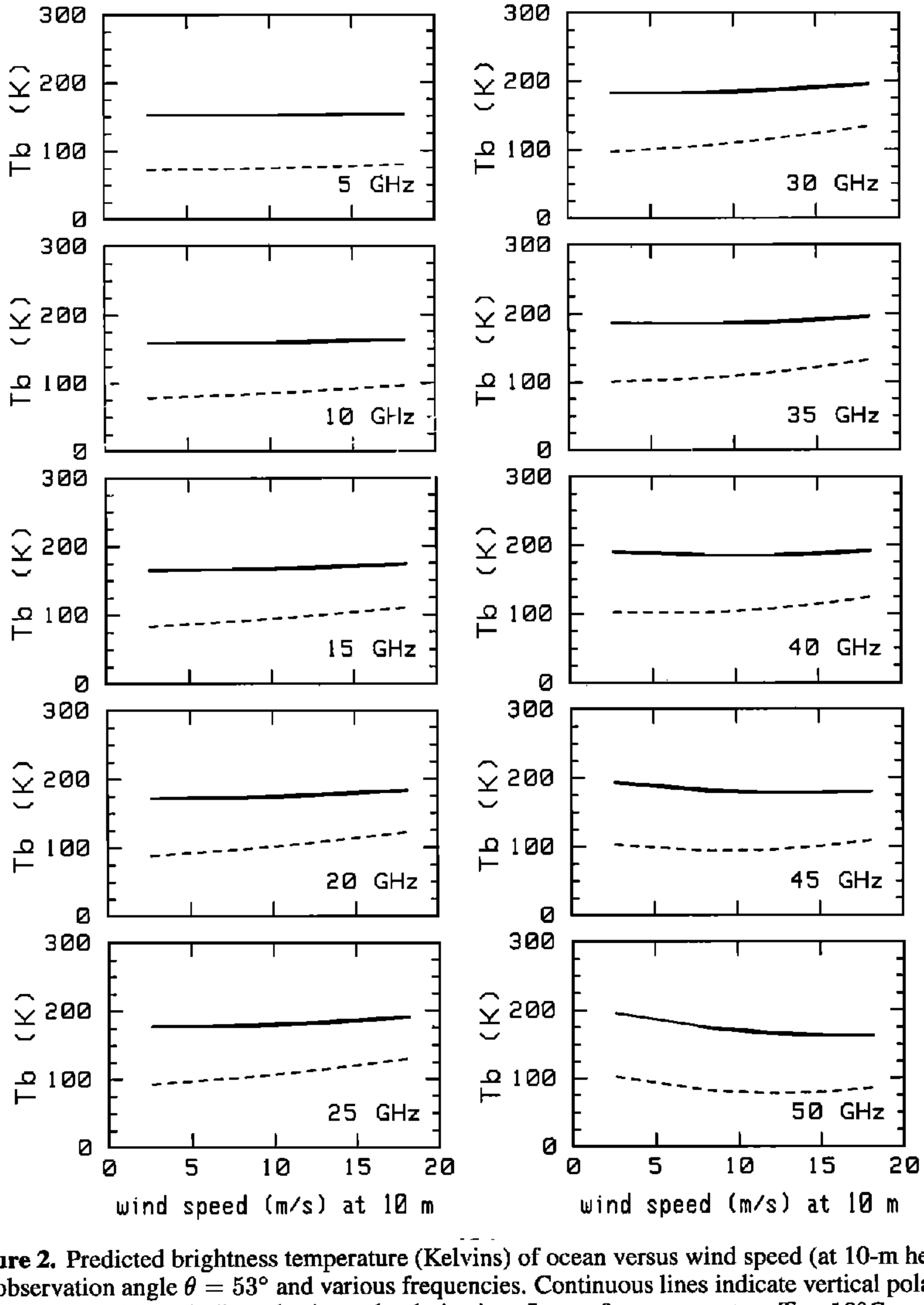

Figure 2. Predicted brightness temperature (Kelvins) of ocean versus wind speed (at 10-m height) for observation angle $\theta = 53°$ and various frequencies. Continuous lines indicate vertical polarization, and dashed lines indicate horizontal polarization. Sea surface temperature $T = 18°C$.

the considerable sparseness of radiosonde launching sites in the oceanic areas. In this case, elongated stripes of homogeneous atmosphere with generally constant-latitude borders have been assumed around the marine radiosonde stations.

Since the elevation of the radiosonde launching sites in general differed from the mean elevation of the land pixels, the profiles of meteorological variables were either extrapolated following the corresponding reference atmosphere height profiles [*Damosso et al.*, 1983] or cut off, according to the specific needs.

To simulate the effect of liquid water, an effective nonprecipitating cloud with base at 1 km above the surface and 3 km thick and with a liquid water density given by

the *Decker et al.* [1978] model has been assumed. The fraction of pixel area covered by the effective cloud has been computed from the ratio between the integrated liquid content of the atmosphere over the considered parcel and the effective-cloud liquid content, so that the portion of the pixel covered by clouds is proportional to the local value of atmospheric liquid.

4. Emission From the Surface-Atmosphere System

To estimate the emission observed from space, the contribution of the surface must be combined with the atmospheric one, and the surface/atmosphere interaction must be evaluated. Emission from the surface is computed by use of the emissivity models reported in section 2 for each surface type, assuming the proper surface temperature. The values of the latter for the sea have been obtained from the already mentioned monthly mean sea surface temperature [*Reynolds and Smith*, 1994] database and, for land, from the 6-hourly surface temperature database for the years 1987 and 1988 [*European Centre for Medium-Range Weather Forecasts*, 1995].

The attenuation and the upward and downward emission of the atmosphere are computed at the desired frequency and elevation angle by using the millimeter-wave propagation model (MPM) of *Liebe et al.* [1993], fed by the seasonally averaged temperature and water vapor profiles measured by the radiosondes and by the seasonal liquid profile associated with the effective cloud.

The computed quantities are then combined to yield the global brightness temperatures of each Earth parcel at the needed sensor parameters by using equation (2), already discussed in section 1.

5. Comparison With Experimental Data

To validate our global model, a global experimental data set, such as the one provided by the Defense Meteorological Satellite Program special sensor microwave imager (SSM/I) [*Remote Sensing Systems*, 1993], was required. To this end, the SSM/I measurements covering the entire year 1992 taken by the 19-, 22-, and 37-GHz channels have been selected as the reference "radiometric truth" data set. The calibrated and quality-checked brightness temperatures have been assigned to the $1° \times 1°$ Earth parcels and averaged over the four groups of 3 months corresponding to the seasons.

To compare model and satellite data, the theoretical brightness temperatures have been computed at the same observation angle ($\theta = 53°$), frequencies, and polarizations at which the SSM/I data are taken. The computations have been carried out separately for each "season" by taking into account both the eventual seasonal variations of surface characteristics and the changes of the atmospheric parameters.

A comparison on a seasonal pixel-by-pixel basis of the theoretically estimated brightness temperatures against the experimental ones has been carried out, and a number of discrepancies between model and measured data have been noted for each radiometric channel. On the basis of these observations, several remedies have been worked out to reduce these discrepancies, by modifying the originally modeled emitting scenario.

As far as the surface is concerned, in some cases mixed surface types have been considered, to reproduce both the spatial inhomogeneities unavoidably present in the $1° \times 1°$ pixels and the temporal ones. Surface parameters relevant to emission were also suitably tuned, when needed. In other cases, slight modifications of the emissivity models have been found appropriate to reproduce the observed frequency and/or polarization dependence with a better accuracy.

Adjustments of the local atmospheric contours were appropriate over the oceans, where radio sounding stations are sparse. We considered the sets of data taken by radiosondes launched from marine locations and, for a given pixel, we identified the one that minimized the rms difference ΔT_B between theoretical and experimental brightness temperature for all radiometric frequencies and polarizations and all "seasons." These data were selected to represent the atmospheric features over the pixels in the oceanic areas. To reduce possible artifacts, the procedure was constrained both by imposing the condition that the latitude of the pixel and the one of the radio sounding site not differ by more than 60° and that if soundings from more than one site gave ΔT_B within 10%, the site closest to the pixel was selected.

After the above modifications and adjustments, the final model of emission producing the brightness temperatures at the various frequencies and polarizations for the four considered "seasons" has been obtained. Plate 1 shows an example of the brightness temperature maps obtainable by the model compared with the one measured by the SSM/I. Theoretical and measured maps reveal appreciable agreement also in rather fine details. The emission model reproduces many relevant features of T_B, both over land, where the atmospheric contribution is less apparent, and over the oceans, where the contrast between the low emission from the water surface and the atmo-

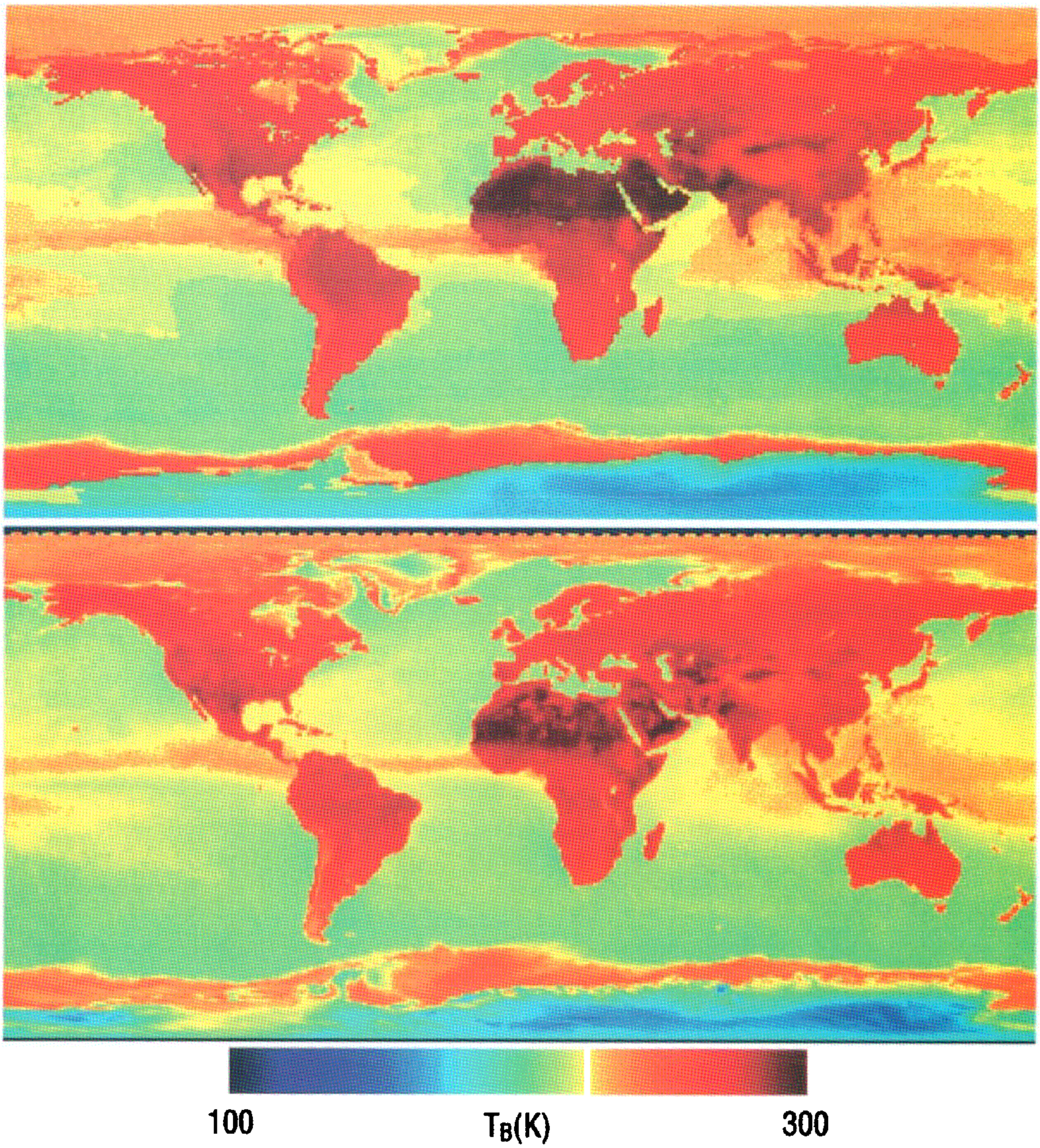

Plate 1. (top) Theoretical and (bottom) experimental maps of the brightness temperatures at 37 GHz, vertical polarization, for boreal summer.

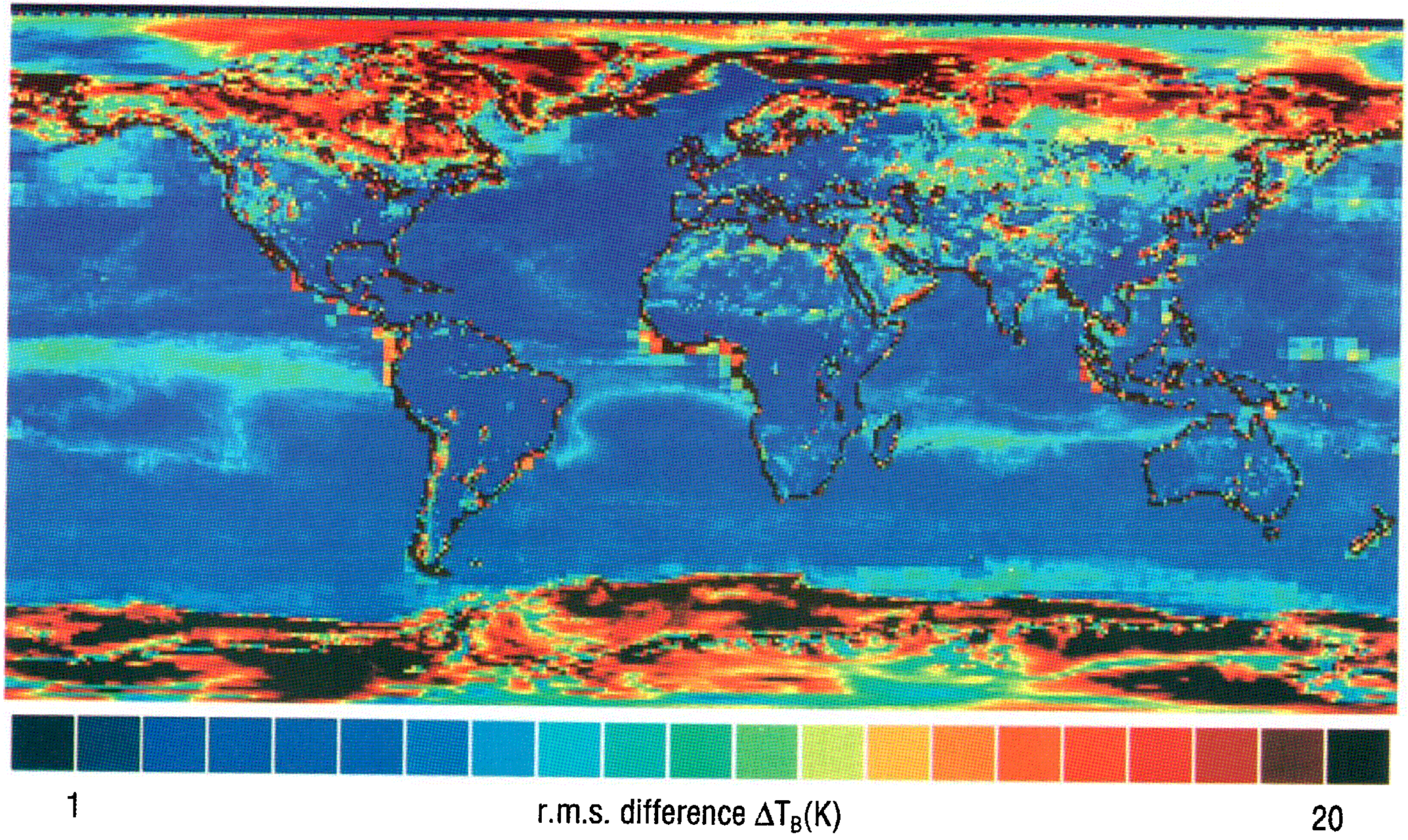

Plate 2. Map of rms difference between theoretical and experimental brightness temperatures computed for all seasons and special sensor microwave imager channels (85 GHz excepted).

spheric one enhances the effects of water vapor and cloud liquid. Larger discrepancies can be noted in the polar regions, probably due to inadequacies both of the emissivity models of ice and snow and of the surface characterization.

The emission model performance can be quantitatively assessed by comparing theoretical and SSM/I T_B through two different approaches. In the first approach, we globally evaluate the accuracy of estimates for the various types of surface at the corresponding geographic locations. In the second, we evaluate the accuracy of estimates for each frequency, polarization, and season, globally for the whole Earth.

Plate 2 epitomizes the results through a map of the comprehensive rms ΔT_B difference computed by averaging over frequencies, polarizations, and seasons. The error appears low for areas with well-developed vegetation (especially tropical forest) and midlatitude oceans. The considerable convective activity in the Intertropical Convergence Zone increases the discrepancy over the ocean at low latitudes. Similarly, the storms which develop at the high latitudes of northern and southern oceanic areas seem to increase the error, probably due to the effects of both the atmosphere and the rough sea surface. The highest discrepancies are produced by glacier and sea ice and by snow. Emission from continental ice over Green-

Table 1. Experimental and Theoretical Global Average Brightness Temperatures and RMS Difference for the Four Seasons

Channel	Experimental T_B	Theoretical T_B	RMS Difference
	Boreal Spring (rms total = 8.39)		
19V	221.36	220.44	6.58
19H	173.92	176.95	10.03
22V	238.48	236.20	7.25
37V	229.99	231.89	6.98
37H	189.44	190.07	10.34
	Boreal Summer (rms total = 8.19)		
19V	223.37	222.89	6.90
19H	176.62	180.14	10.79
22V	240.67	238.77	7.04
37V	232.76	234.17	5.71
37H	192.83	192.92	9.46
	Boreal Autumn (rms total = 8.86)		
19V	221.25	221.17	7.32
19H	174.06	178.14	11.93
22V	237.87	236.74	7.48
37V	230.38	232.55	6.29
37H	190.22	191.27	10.04
	Boreal Winter (rms total = 8.53)		
19V	219.43	218.96	6.56
19H	171.56	175.31	10.56
22V	236.53	234.73	7.16
37V	227.87	230.21	7.16
37H	187.08	188.46	10.35

All values are given in Kelvins.

land and Antarctic is found to be generally overestimated, while the large time variability of the surface-emitting properties of sea ice and of snow-covered regions is believed to be mainly responsible for the considerable errors appearing in the Arctic, over northern Canada and northern Siberia, and close to the Antarctic coast.

Table 1, in turn, compares the global (averaged over all surface pixels) theoretical brightness temperatures with the experimental ones and reports the rms deviations between model and observed T_B over all pixels, leaving out the coastal ones, for which the experimental data correspond to a mixed sea-land surface. Data in Table 1 point out that the emission at vertical polarization is predicted more accurately than the the one at horizontal polarization, almost irrespective of frequency and season. The 19H channel exhibits the highest discrepancy. A comparison between predicted and experimental T_B maps at this frequency and polarization reveals that emission from the sea surface is generally underestimated, especially in the northern and southern zones of the oceans. Emission from continental ice (Greenland and Antarctic) also is strongly underestimated, whereas snow-covered areas appear considerably warmer than predicted. Moreover, a slight underestimate is detected in arid areas, like the Sahara, Kalahari, Neged, and Gibson Deserts.

Finally, the emission model has been used in antenna temperature predictions, performed by integrating the particular antenna pattern over the brightness temperature distribution. A sample contoured beam from the EUTELSAT II FM6 antenna has been used for a validation test case, in which the theoretical antenna temperature has been compared with in-orbit measurements.

In the considered case, the predicted value (T_A = 145.9 K) was found to differ by less than 0.1 dB from the measured one [*Schiavon et al.*, 1996].

6. Conclusions

A global emission model of the whole Earth has been implemented in order to predict its local microwave brightness temperature in a wide range of frequencies and observation angles at vertical and horizontal polarizations. The model, which results from an effort to transfer the considerable know-how gained in remote sensing into telecommunications, is well suited for estimating the uplink gain-to-noise ratio of satellite-borne receivers for a variety of orbital locations and antenna patterns, including narrow beams. Applications to Earth observation can be envisaged also, for the retrieval of both surface and atmospheric parameters from radiometric measurements. The comparison between predicted and in-orbit measured antenna temperatures indicates that the model performs well for telecommunications purposes. However, the discrepancies noted between theoretical and measured brightness temperatures at some frequencies and polarizations suggest that further tuning of the emission models of particular types of surface, including sea water, ice, snow, and arid land, might be advisable.

Acknowledgments. This paper summarizes results obtained in a study carried out under a contract from ESA/ESTEC (TICRA, Copenhagen, Denmark, prime contractor), monitored by S. Badessi. Radiosonde and integrated liquid content databases were kindly provided by F. Barbaliscia's group at Fondazione Ugo Bordoni. Leila Guerriero made available the two-scale emission model of the ocean. The authors thank the Data Assimilation Office (Code 910.3) and the Distributed Archive Center (Code 902.2) at the Goddard Space Flight Center, Greenbelt, Maryland, for producing and distributing the ocean wind speed data. The latter activities were sponsored by NASA's Mission to Planet Earth Program.

References

Barbaliscia, F., M. Boumis, and A. Martellucci, Study of scaling of propagation effects from microwave to optical frequencies, *ESA-ESTEC Contract 10195/92/NL/GS*, final report, Eur. Space Res. and Technol. Cent., Noordwijk, Netherlands, October 1995.

Borgeaud, M., E. Attema, G. Salgado-Gispert, A. Bellini, and J. Noll, Analysis of bare soil surface parameters with ERS-1 SAR data, in *Proceedings of the International Symposium on Retrieval of Bio- and Geophysical Parameters from SAR Data for Land Applications*, pp. 307–316, CNES, Tolouse, France, 1995.

Coppo, P., et al., A physical model for ocean wind measurements by means of radiopolarimetry, paper presented at the Fifth Specialist Meeting on Microwave Radiometry and Remote Sensing of the Environment, Boston, Mass., Nov. 4–6, 1996.

Damosso, E., L. Stola, and G. Brussaard, Characterization of the 50–70 GHz band for space communications, *ESA J.*, *7*, 25–43, 1983.

Decker, M.T., E.R. Westwater, and F.O. Guiraud, Experimental evaluation of ground-based microwave radiometric sensing of atmospheric temperature and water vapor profiles, *J. Appl. Meteorol.*, *17*, 1788–1795, 1978.

DeFries, R.S., and J.R.G. Townshend, NDVI-derived land cover classification at global scales, *Int. J. Remote Sens.*, *15*, 3567–3586, 1994.

de Maagt, P.J.I., S. Badessi, and H.T. Fenech, Antenna temperature and G/T assessment for receive satellite antennas with regional coverage, in *Journées Internationales de Nice sur les Antennes (JINA)*, 366–369, Cent. Natl. d'Etudes des Télécommun., Paris, 1994.

Dzura, M.S., V.S. Etkin, A.S. Khrupin, M.N. Pospelov, and M.D. Raev, Radiometers-polarimeters: principles of design and applications for sea surface microwave emission polarimetry, in *Proceedings of 1994 International Geoscience and Remote Sensing Symposium*, pp. 1432–1434, IEEE, Piscataway, New Jersey, 1994.

Ellison, W.J., A. Balana, G. Delbos, K. Lamkaouchi, L. Eymard, C. Guillou, and C. Prigent, Study and measurement of the dielectric properties of Sea Water, *ESA/ESTEC Contract 11197/94/NL/CN*, final report, Eur. Space Res. and Technol. Cent., Noordwijk, Netherlands, 1996.

European Centre for Medium-Range Weather Forecasts, *The Description of the ECMWF/WCRP Level III-A Global Atmospheric Data Archive*, Oper. Dep., Shinfield Park, Reading, England, 1995.

Fenech, H.T., B. Kasstan, A. Lindley, P.J.I. de Maagt, and S. Badessi, G/T predictions of communication satellites based on a new Earth brightness model, *Int. J. Satell. Commun.*, *13*, 367–376, 1995.

Ferrazzoli, P., and L. Guerriero, Modeling microwave emission from vegetation-covered surfaces: A parametric analysis, in *Passive Microwave Remote Sensing of Land-Atmosphere Interactions*, edited by B.J. Choudhury et al., pp. 389–402, VSP Press, Utrecht, Netherlands, 1995.

Ferrazzoli, P., and L. Guerriero, Passive microwave remote sensing of forests: A model investigation, *IEEE Trans. Geosci. Remote Sens.*, *34*, 433–443, 1996.

Ferrazzoli, P., L. Guerriero, and D. Solimini, Numerical model of microwave backscattering and emission from terrain covered with vegetation, *Appl. Comput. Electromagn. Soc. J.*, *6*, 175–191, 1991a.

Ferrazzoli, P., D. Solimini, G. Luzi, and S. Paloscia, Model analysis of backscatter and emission from vegetated terrain, *J. Electromagn. Waves Appl.*, *5*, 175–193, 1991b.

Ferrazzoli, P., L. Guerriero, S. Paloscia, and P. Pampaloni, Modeling X and K_a band emission from leafy vegetation, *J. Electromagn. Waves Appl.*, *9*, 343–406, 1995.

Foster, D.J., and R.D. Davy, Global snow depth climatology, *Rep. USAFETAC/TN-88/006*, 48 pp., Scott Air Force Base, Ill., 1988.

Fung, A.K., *Microwave Scattering and Emission Models and Their Applications*, Artech House, Norwood, Mass., 1994.

Guerriero, L., and C. Mätzler, A model and experiments for microwave radiometry of forests, in *Proceedings of the Specialist Meeting on Microwave Radiometry and Remote Sensing of the Environment*, pp. 401-409, VSP Press, Utrecht, Netherlands, 1995.

Hollinger, J.P., Passive microwave measurements of sea surface roughness, *IEEE Trans. Geosci. Remote Sens.*, *GE-9*, 165–169, 1971.

Imhoff, M.L., Radar backscatter and biomass saturation: Ramifications for global biomass inventory, *IEEE Trans. Geosci. Remote Sens.*, *33*, 511–518, 1995.

Liebe, H.J., G.A. Hufford, and M.G. Cotton, Propagation modeling of moist air and suspended water/ice particles at frequencies below 1000 GHz, in *AGARD 52nd Specialists' Meeting of the Electromagnetic Wave Propagation Panel*, pp. 3.1–3.10, AGARD, Loughton, Essex, 1993.

Mätzler, C., Passive microwave signatures of landscapes in winter, *Meteorol. Atmos. Phys.*, *54*, 241–260, 1994a.

Mätzler, C., *Passive Microwave Signature Catalog*, Univ. of Bern, Bern, Switzerland, 1994b.

Meeson, B.W., F.E. Coprew, J.M.P. Mcmanus, D.M. Myers, J.W. Closs, K.-J. Sun, D.J. Sunday, and P.J. Sellers, ISLSCP Initiative I global data sets for land-atmosphere models, 1987–1988, vol. 1–5, [CD USA_-NASA_GDAAC_ISLSCP_001/USA_NASA_GDAAC_-ISLSCP_005], NASA Goddard Distributed Active Archive Center (DAAC), Greenbelt, Maryland, 1995.

Noll, J., J.P.V. Poiares Baptista, and M. Borgeaud, Emissivity of snow-covered terrains for spaceborne applications, in *Proceedings of 1995 International Geoscience and Remote Sensing Symposium*, pp. 716–718, IEEE, Piscataway, New Jersey, 1995.

Paloscia, S., P. Pampaloni, L. Chiarantini, P. Coppo, S. Gagliani, and G. Luzi, Multifrequency passive microwave remote sensing of soil moisture and roughness, *Int. J. Remote Sens.*, *14*, 467–483, 1993.

Pampaloni, P., and S. Paloscia, Microwave emission and plant water content: A comparison between field measurements and theory, *IEEE Trans. Geosci. Remote Sens.*, *GE-24*, 900–905, 1986.

Pandey, P.C., and R.K. Kakar, An empirical microwave emissivity model for a foam-covered sea, *IEEE J. Oceanic Eng.*, *OE-7*, 135–140, 1982.

Remote Sensing Systems, User's manual SSM/I antenna temperature tapes, *RSS Tech. Rep. 120193*, Santa Rosa, Calif., December 1993.

Reynolds, R.W., and T.M. Smith, Improved global sea surface temperature analyses, *J. Clim.*, *7*, 929–948, 1994.

Rott, H., Multispectral microwave signatures of the Antarctic ice sheet, in *Microwave Radiometry and Remote Sensing Applications*, edited by P. Pampaloni, pp. 89–101, VSP Press, Utrecht, Netherlands, 1989.

Schiavon, G., P. Ferrazzoli, R. Jørgensen, S. Badessi, P. de Maagt, and H. Fenech, Estimate of antenna noise temperature by using detailed earth surface and atmospheric emissivity data, in *Journées Internationales de Nice sur les antennes (JINA)*, pp. 544–547, Cent. Natl. d'Etudes des Télécommun., Paris, 1996.

Schubert, S.D., J. Pjaendtner, and R. Hood, An assimilated data set for Earth science applications, *Bull. Am. Meteorol. Soc.*, *74*, 2331–2342, 1993.

Sellers, P.J., S.O. Los, C.J. Tucker, C.O. Justice, D.A. Dazlich, G.J. Collatz, and D.A. Randall, A global 1 by 1 degree NDVI data set for climate studies, 2, The generation of global fields of terrestrial biophysical parameters from the NDVI, *Int. J. Remote Sens.*, *15*, 3519–3545, 1994.

Sellers, P.J., et al., An overview of the ISLSCP Initiative I global data sets for land-atmosphere models, 1987–1988, vol. 1–5, [CD vol. 1, USA_NASA_GDAAC_-ISLSCP_001, OVERVIEW.DOC], NASA Goddard Distributed Active Archive Center (DAAC), Greenbelt, Maryland, 1995.

Sellers, P.J., S.O. Los, C.J. Tucker, C.O. Justice, D.A. Dazlich, G.J. Collatz, and D.A. Randall, A revised land surface parameterization (SiB2) for atmospheric GCMs, 2, The generation of global fields of terrestrial biophysical parameters from satellite data, *J. Clim.*, *9*, 706–737, 1996.

Shutko, A. M., and A.A. Chukhlantsev, Microwave radiation peculiarities of vegetative covers, *IEEE Trans. Geosci. Remote Sens.*, *GE-20*, 27–29, 1982.

Sume, A., C. Mätzler, R. Hüppi, and E. Schanda, "Microwave radiometer and scatterometer measurements of vegetation", *FOA Rep. C 30494-3.2*, Linköping, Sweden, 1988.

Trokhimovski, Y.G., G. Bolotnikova, V. Etkin, S. Grechko, and A. Kuzmin, The dependence of S-band sea surface brightness temperature on wind vector at normal incidence, *IEEE Trans. Geosci. Remote Sens.*, *33*, 1085–1088, 1995.

Troy, B.E., J.P. Hollinger, R.M. Lerner, and M.M. Wisler, Measurement of the microwave properties of sea ice at 90 GHz and lower frequencies, *J. Geophys. Res.*, *86*, 4283–4289, 1981.

Ulaby, F. T., R. K. Moore, and A. K. Fung, *Microwave Remote Sensing: Active and Passive*, vol. II, *Surface Scattering and Emission Theory*, Addison-Wesley, Reading, Mass., 1982.

Ulaby, F. T., R. K. Moore, and A. K. Fung, *Microwave Remote Sensing: Active and Passive*, vol. III, *From Theory to Applications*, Artech House, Norwood, Mass., 1986.

Wang, J.R., P.E. O'Neill, T.J. Jackson, and E.T. Engman, Multifrequency measurements of the effects of soil moisture, soil texture, and surface roughness, *IEEE Trans. Geosci. Remote Sens.*, *GE-21*, 44–51, 1983.

Wegmüller, U., Remote sensing signature studies on agricultural fields with ground-based radiometry and scatterometry, Ph.D. thesis, Univ. of Bern, Bern, Switzerland, 1990.

Wilheit, T.T., A model for the microwave emissivity of the ocean's surface as a function of wind speed, *IEEE Trans. Geosci. Remote Sens.*, *GE-17*, 244–249, 1979.

Wilheit, T.T., W. Nordberg, J. Blinn, W. Campbell, and A. Edgerton, Aircraft measurements of microwave emission for Arctic sea ice, *Remote Sens. Environ.*, 2, 129–139, 1972.

Wilheit, T.T., et al., Algorithms for the retrieval of rainfall from passive microwave measurements, *Remote Sens. Rev.*, *11*, 163–194, 1994.

Yueh, S.H., W.J. Wilson, F.K. Li, S.V. Nghiem, and W.B. Ricketts, Polarimetric measurements of sea surface brightness temperatures using an aircraft K-band radiometer, *IEEE Trans. Geosci. Remote Sens.*, *33*, 85–92, 1995.

P. de Maagt and J.P.V. Poiares Baptista, ESA/ESTEC, XEP, Keplerlaan, 2200 AG, Noordwijk, Netherlands. (e-mail: pdemaagt@estec.esa.nl; pedro@xe.estec.esa.nl)

P. Ferrazzoli, G. Schiavon, and D. Solimini, Università Tor Vergata, D.I.S.P., Via di Tor Vergata, I-00133, Roma, Italy. (e-mail: ferrazzoli@utovrm.it; schiavon@disp.utovrm.it; solimini@disp.utovrm.it)

(Received March 7, 1997; revised July 28, 1997; accepted August 15, 1997.)